**Atmospheric
Measurement
Techniques**

Spatial resolution of tropical terrestrial CO₂ fluxes inferred using space-borne column CO₂ sampled in different earth orbits: the role of spatial error correlations

P. I. Palmer[1], L. Feng[1], and H. Bösch[2]

[1]School of GeoSciences, University of Edinburgh, King's Buildings, Edinburgh, EH9 3JN, UK
[2]Department of Physics and Astronomy, University of Leicester, Leicester, UK

Abstract. We use realistic numerical experiments to assess the sensitivity of 8-day CO_2 flux estimates, inferred from space-borne short-wave infrared measurements of column-averaged CO_2 dry air mixing ratio X_{CO_2}, to the choice of Earth observing orbit. We focus on three orbits: (1) a low-inclination circular orbit used by the NASA Tropical Rainfall Measuring Mission (TRMM); (2) a sun-synchronous orbit used by the Japanese Greenhouse Gases Observing SATellite (GOSAT) and proposed for the NASA Orbiting Carbon Observatory (OCO-2) instrument; and (3) a precessing orbit used by the International Space Station (ISS). For each orbit, we assume an instrument based on the specification of the OCO-2; for GOSAT we use the relevant instrument specification. Sun-synchronous orbits offer near global coverage within a few days but have implications for the density of clear-sky measurements. The TRMM and ISS orbits intensively sample tropical latitudes, with sun-lit clear-sky measurements evenly distributed between a.m./p.m. For a specified spatial resolution for inferred fluxes, we show there is a critical number of measurements beyond which there is a disproportionately small decrease in flux uncertainty. We also show that including spatial correlations for measurements and model errors (of length 300 km) reduces the effectiveness of high measurement density for flux estimation, as expected, and so should be considered when deciding sampling strategies. We show that cloud-free data from the TRMM orbit generally can improve the spatial resolution of CO_2 fluxes achieved by OCO-2 over tropical South America, for example, from 950 km to 630 km, and that combining data from these low-inclination and sun-synchronous orbits have

the potential to reduce this spatial length further. Decreasing the length of the error correlations to 50 km, reflecting anticipated future improvements to transport models, results in CO_2 flux estimates on spatial scales that approach those observed by regional aircraft.

1 Introduction

Changes in the atmospheric concentration of carbon dioxide (CO_2) reflect changes in the net balance of regional ocean and terrestrial (including natural vegetation, and the incomplete combustion of biomass and fuel) fluxes. Natural land-based and ocean fluxes represent large components to the atmospheric CO_2 budget but they are associated with substantial uncertainty about their location, strength, and durability (Le Quere et al., 2009). Without proper characterisation of these natural fluxes it is impossible to move far forward with establishing a robust emission verification scheme that is critical in reducing global greenhouse gas emissions.

Quantifying the natural terrestrial fluxes, in particular, is hampered by poor accessibility and large spatial heterogeneity, especially over tropical and boreal ecosystems, so that the small amount of precise ground-based data is inadequate for quantifying surface-atmosphere CO_2 fluxes (e.g. Gurney et al., 2002; Le Quere et al., 2009). Space-borne instruments that measure short-wave infrared radiation (SWIR) represent a partial solution to this problem by providing a large volume of indirect measurements of atmospheric CO_2 with lower precision than in situ sensors. Previous work has evaluated the ability of different concepts, including instruments that measure SWIR (OCO, GOSAT, SCIAMACHY) and thermal IR (AIRS, IASI), and active

instruments (LIDAR), to globally monitor CO$_2$ fluxes compared to the existing (and an enhanced) ground-based surface network (Hungershoefer et al., 2010). This study concluded that even with the large reductions in flux uncertainties associated with these observing concepts they still not meet the demanding requirements associated with monitoring carbon fluxes, and that these systems should focus on fluxes linked to vegetation and land ecosystem dynamics.

The main science objective of our experiments is to estimate surface CO$_2$ fluxes on sub-continental spatial scales over tropical ecosystems from space-based X_{CO_2} measurements obtained in different orbital configurations (Sect. 2). Current and planned space-borne instruments specifically designed to measure CO$_2$ (e.g. OCO-2 or GOSAT) have chosen a sun-synchronous orbit that samples airmasses at latitudes as high as 82°. These orbits have the advantage that the global atmosphere is sampled within a few days but it has implications for the number of measurements available at any one latitude and longitude over a fixed period of time, and consequently for the spatial and temporal resolution of inferred surface fluxes.

In Sect. 4, we show that the choice of Earth observing orbits, which has implications for the spatial and temporal measurement coverage and density, affects the extent to which our primary science objective can be achieved, as expected (Miller et al., 2007). For our experiments, we assume a grating spectrometer that has the same technical specifications as the NASA Orbiting Carbon Observatory-2 (Crisp et al., 2004); with the exception of the GOSAT for which we use the appropriate technical specification. Using our flux estimation calculations (described in Sect. 3), we show that for a particular spatial resolution of flux estimate there is a critical number of measurements beyond which the decrease in uncertainty of inferred fluxes is disproportionately small; and that including spatial correlations for measurement and model error decreases the effectiveness of high-density measurements. We show that using an instrument in a low inclination orbit reduces the spatial coverage of the data but increases the spatial and temporal resolution of the independent flux estimates. We also report the complementarity offered by combining data from instruments in a low inclination orbit and one in sun-synchronous orbit. We conclude the paper in Sect. 5.

2   Mission concepts

For all but one of our experiments, we assume access to an instrument that closely matches the publicly available technical specifications of the OCO-2 instrument; for comparison, we also use an instrument with the technical specification of GOSAT. The OCO-2 platform includes three, high-resolution grating spectrometers that measure absorptions of the reflected sunlight by using two CO$_2$ bands (1.61 and 2.06 µm) and the O$_2$ A-Band (0.765 µm) using nadir-viewing

geometry and glint-viewing geometry, where the instrument points to the spot where solar radiation is specularly reflected from the surface (Crisp et al., 2004). Glint-view measurements are particularly important over the ocean (which appears dark in the nadir) because they have high signal to noise, but they generally have a slightly larger surface footprint and a longer atmospheric path compared to nadir measurements (Crisp et al., 2004; Miller et al., 2007). Previous work has showed that the glint measurements of tropical continental outflow over the oceans, if retrieved with sufficient accuracy, are more effective at inferring tropical CO$_2$ fluxes than nadir measurements over land which are subject to seasonal clouds and biomass burning aerosol (Feng et al., 2009; Baker et al., 2010).

The GOSAT platform consists of the cloud aerosol imager (CAI) and a SWIR/thermal IR (TIR) Fourier Transform spectrometer which measures similar parts of the SWIR spectrum to OCO-2 with an additional 5.56–14.3 µm channel (Kuze et al., 2009). Individual soundings have an integration time of 4 s, and are spaced by $\simeq$150 km. Unlike the OCO-2 instrument, which is pointed by the spacecraft, the GOSAT spectrometer is mounted on a nadir-pointed spacecraft and uses a dedicated pointing mechanism that can only view scenes within $\simeq$20° of the local nadir. It therefore cannot view the glint spot when it is more than $\simeq$20° from the sub-solar latitude.

We consider three individual orbits for the OCO-2 instrument: (1) a sun-synchronous orbit with an afternoon overpass time similar to the one proposed by NASA for OCO-2; (2) a low-inclination orbit, previously used by the NASA TRMM platform; and (3) a low-inclination orbit used by the International Space Station (ISS). For brevity, hereinafter, these orbits will be referred to as OCO-2, TRMM, and ISS, respectively. We use the GOSAT orbital parameters for the GOSAT calculation. Table 1 shows the orbital parameters we use to define each orbit. For our calculations, we assume that the ISS has sufficient stability to support the pointing requirements for CO$_2$ measurements; we acknowledge this is a bold assumption but the ISS offers a useful and alternative platform with which to compare results from using more conventional platforms. Below, we also present results from combining SWIR CO$_2$ data taken in a OCO-2 and in a TRMM orbit. The orbits we use are described by Table 1. We use daily orbit patterns described on a uniform 0.25° lat/lon grid, assuming a sampling of 3 Hz. For OCO-2 (and therefore also for ISS and TRMM concepts that use OCO-2), we do not explicitly assume across track sampling but account for this by scaling the number of observations that fall into the gridded product by 4, which represents the number of cross-track pixels planned for OCO-2.

Table 1. Orbital parameters used to determine mission concepts studied.

Orbit/Instrument Characteristic	OCO-2[1]	GOSAT	TRMM	ISS
Type	SS[2]	SS	circular	
Local overpass time	13.30 (asc[3])	13.15 (desc[4])	precesses	precesses
Altitude [km]	705	666	400	345
Ground speed [km s^{-1}]	7.5	7.5	7.65	7.67
Inclination [deg]	98.2	98.1	35.0	51.6
Period [min]	98.8	100	92.6	91.5
Revolutions/day	14.6	14.6	15.6	15.7
Nadir footprint	3 km^2	10 km diameter	1.5 km^2	1.4 km^2
(along- × across-track)	2.2 × 1.3 km^2		2.2 × 0.68 km^2	2.2 × 0.64 km^2

[1] Based on orbit of the NASA Aqua platform; [2] SS = sun-synchronous; [3] asc = ascending node; [4] desc =,descending node.

3 Forward and inverse model description

We use Observing Simulation System Experiments (OSSEs) to determine the potential of space-borne X_{CO_2} data to improve weekly surface CO$_2$ flux estimates. For brevity we only include a brief description of the OSSE infrastructure used, and refer the reader to Feng et al. (2009) for further details.

We use the GEOS-Chem model (v7.03.06) to relate the surface state (fluxes) to the retrieved measurements of CO$_2$ dry-air mole fractions X_{CO_2}. We use the model with a horizontal resolution of 2° × 2.5° and 30 vertical levels (derived from the native 48 levels) ranging from the surface to the mesosphere, 20 of which are below 12 km. The model is driven by GEOS-4 assimilated meteorology data from the Global Modeling and Assimilation Office Global Circulation Model based at NASA Goddard. The 3-D meteorological data are updated every 6 h, and the mixing depths and surface fields are updated every three hours. We use data from 2003 to represent a typical year; we do not anticipate that using different years will significantly change our results.

We use prior flux inventories for biomass burning (van der Werf et al., 2006), anthropogenic activity (Marland et al., 2007), biofuel combustion (Yevich and Logan, 2003), land biosphere (Randerson et al., 1997), and the oceans (Takahashi et al., 2009) to produce global 3-D fields of atmospheric CO$_2$. This model has been recently evaluated using surface, aircraft and satellite measurements of CO$_2$ (Feng et al., 2011). We linearly decompose our total CO$_2$ concentration into contributions from 144 regions that span the globe (Fig. 1), based on the 22 regions used by TransCom-3 (T3) (Law et al., 2003; Gurney et al., 2002). We divide each T3 land region into 9 near-equal areas (resulting in 9×11 land regions), and divide each T3 ocean region into 4 near-equal areas (resulting in 4 × 11 ocean regions). We have included one region (region 1) to represent all other low-emission regions, typically covered by snow.

We sample the model along the orbits defined in Table 1, and remove cloudy and aerosol-laden scenes (AOD > 0.3). Optical depths are defined according to seasonal probability density functions derived from satellite data (Bösch et al., 2011) for the nominal footprint of each instrument (Table 1). We determine the probability of cloud-free pixels for the different Earth orbits using 3-hourly ECMWF operational analysis for total cloud cover, described with a spatial resolution of 0.25° × 0.25°, accounting for the pixel size, cloud coverage, and an alignment factor between the instrument pixel and the cloud-free sub-grid region. A more detailed description of the method can be found in Appendix A. Very thin cirrus clouds are not explicitly addressed in this calculation mainly because the MODIS satellite data does not have the sensitivity to identify them. In practice, if these clouds are thin enough X_{CO_2} can still be retrieved from the measurements. Thin, high clouds are expected to introduce a clear spectral signature which can also be used to fit such clouds in the retrieval of X_{CO_2}. If we make these assumptions about thin cirrus for the OSSE presented here the only weakness is that we will potentially underestimate the X_{CO_2} error associated with the spectral fitting. GEOS-4 water mole fractions are used to map from CO$_2$ to dry-air mole fraction, and subsequently convolved with scene-specific averaging kernels that account for the vertical sensitivity of the instrument to changes in CO$_2$, resulting in X_{CO_2} (Bösch et al., 2011). Figure 2 shows averaging kernels as a function of viewing model (nadir and glint), five surface types (snow, ocean, soil, conifer, and desert), ten solar zenith angles (from 10° to 85° for glint and from 10° to 72° for glint measurements), and seven aerosol optical depths evenly spaced between 0 and 0.3.

The resulting X_{CO_2} fields represents the "true" atmospheric state observed by the instrument. To generate the "model" first-guess atmosphere, we increase the prior flux inventories by 80 % and follow the steps as defined above. We use an ensemble Kalman Filter with a 96-day lag window to estimate 8-day CO$_2$ fluxes over 144 geographical regions
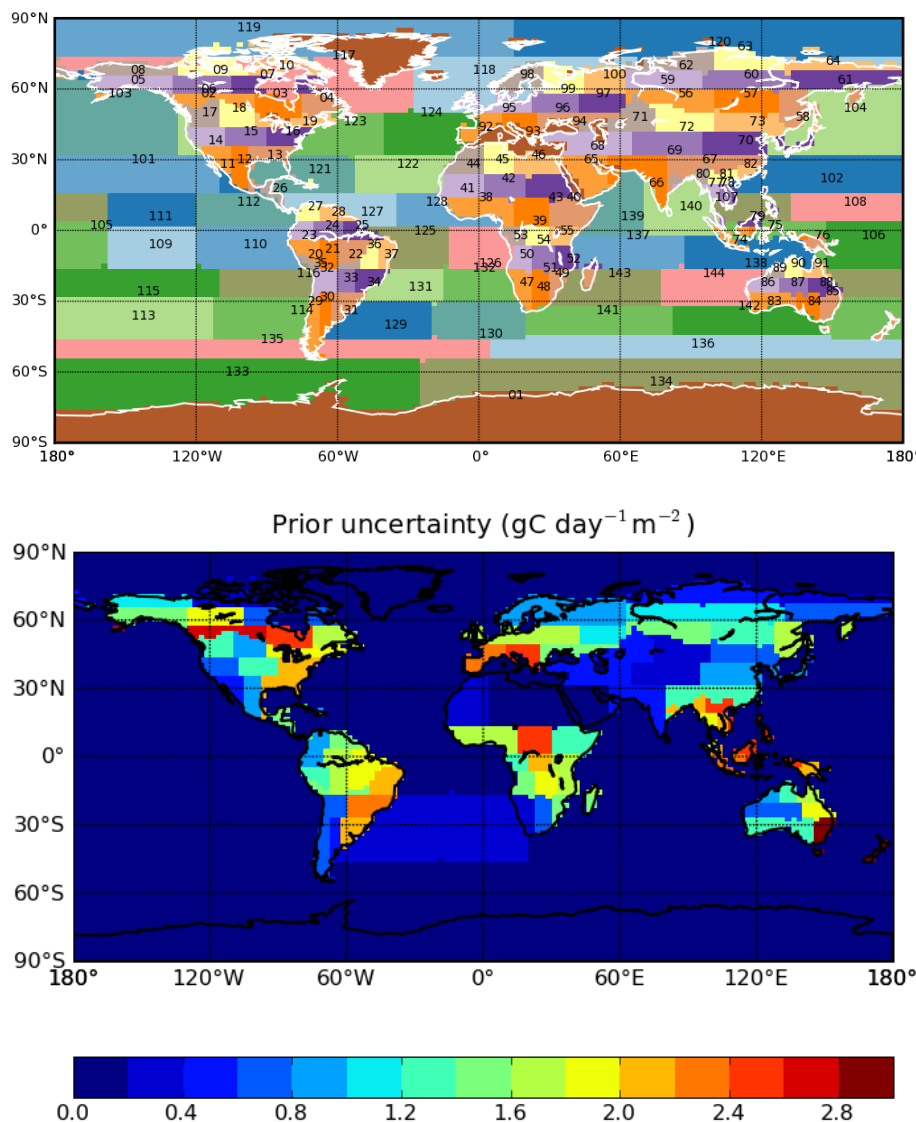
Fig. 1. The continental and ocean regions used to estimate CO$_2$ source and sinks (top panel), and associated prior uncertainties (gC day^{-1} m^{-2} lower panel), based on a coarser distribution from the TransCom-3 experiment (Gurney et al., 2002).

distributed across the globe and based on the TransCom-3 experiments (Feng et al., 2009). For land-based fluxes, a priori uncertainties are assumed to be proportional to the annual net primary production climatology (Patra et al., 2003), with an associated global total of 3.6 GtC yr^{-1}. The uncertainties for ocean fluxes are generated by rescaling their parent T3 regional a priori flux uncertainties (Feng et al., 2009). Figure 3 shows the resulting spatial distribution of the a priori flux uncertainties. We assume the a priori errors have no temporal structure, and we also assume no spatial correlation between these regional flux forecasts, so that their (sub) error covariance matrix is diagonal.

Figure 2 also shows single measurement errors, which are scene-dependent and a function of surface type, solar zenith angle, and aerosol optical depth, as defined above.

As a result of our using a model with a horizontal resolution that is coarser than the measurements we calculate the daily mean of values that fall within individual grid cells of a uniform 1° grid, which have a reduced random error: $\sigma = \sigma_0 \sqrt{1/n + \alpha(1-1/n)}$, where σ_0 is the random error for a single observation, n is the number of clear-sky observations within a 1° × 1° grid, and α is the assumed error correlation coefficient between two observations within that grid box. We assume $\alpha = 0.2$ but find that our results are largely insensitive to the value we adopt because n is typically large. We also include model transport and representation error, which for simplicity, we assume to be 2.0 ppm over land and 1.5 ppm over ocean on a uniform 1° grid based on model intercomparisons (e.g. Chevallier et al., 2010; Feng et al., 2011); these values are consistent with representation errors
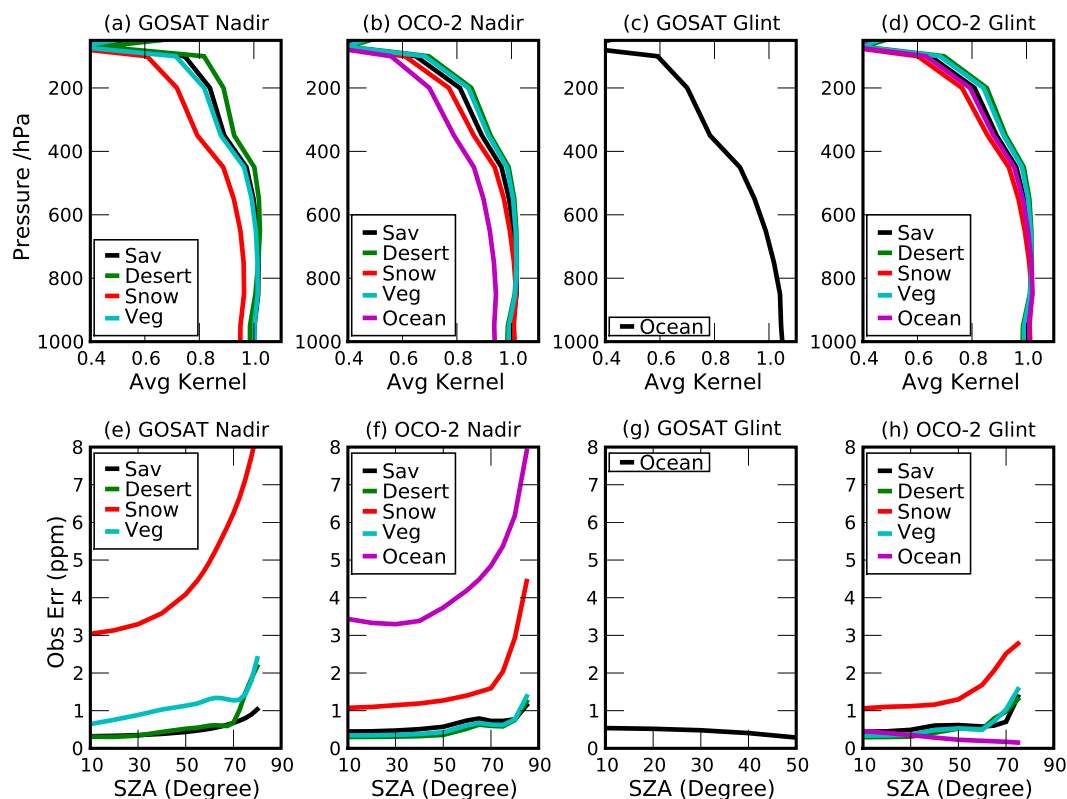
Fig. 2. Averaging kernels (dimensionless, top panels) and single measurement error (ppmv, bottom panels) for nadir and sun-glint viewing modes of the Greenhouse gases. Observing SATellite (GOSAT) and the Orbiting Carbon Observatory (OCO-2) instruments. The averaging kernels are for different land types at a solar zenith angle (SZA) of 10° and an aerosol optical depth (AOD) of 0.1. Observation errors are shown as a function of SZA for different land types and an AOD of 0.1.

estimated from aircraft data (Lin et al., 2004). We assume that model error for individual measurements within one day are spatially correlated, with a correlation length of 300 km. The correlation length scale, chosen to reflect the spatial resolution of the transport model, effectively penalises measurements that are densely distributed over similar horizontal scales. We find that for OCO-2, model error typically dominates the daily mean observation error budget. Similarly, we account for spatial measurement error correlations in the inversion to properly evaluate the impact of data on flux estimates. We show below these correlations must be included to properly evaluate the performances of different instruments over different spatial scales. For our control run we assume a measurement error correlation length of 300 km. We describe a new, efficient method, based on LU decomposition of sparse matrices (Appendix B), of inverting a measurement error covariance matrix that includes these off-diagonal entries. To assess the sensitivity of our results to these assumed model and measurement error correlations we also report results that assume an error correlation length scale of 50 km.

4 Results

Figure 3 shows the number of cloud- and aerosol-free (AOD < 0.3) nadir and glint measurements during January 2003 for the sun-synchronous (OCO-2 and GOSAT), TRMM, and ISS orbits; the number and distribution of corresponding measurements during July 2003 (not shown) reflect seasonal changes in cloud and aerosols. For GOSAT we consider the sum of nadir and glint measurements, reflecting its current mode of operation; for OCO-2, TRMM, and ISS the number of measurements are reported as nadir (glint). The OCO-2 and GOSAT orbits typically results in 40 (45) and 1 clear-sky measurements, respectively, for each 1° grid cell and has near uniform coverage at latitudes <60°; the corresponding random error reflects the distribution of measurements as expected. The ISS orbit typically has 60 (56) measurements for the same 1° × 1° grid but limited to ≃ ±45°; measurement gaps reflect peculiarities of the ISS orbit as well as availability of clear-sky scenes. The low inclination, circular TRMM orbit typically has 81 (85) measurements for the same grid, with generally more cloud-free tropical measurements but limited to ≃ ±30°. The higher frequency of measurements offered by the low-inclination orbit
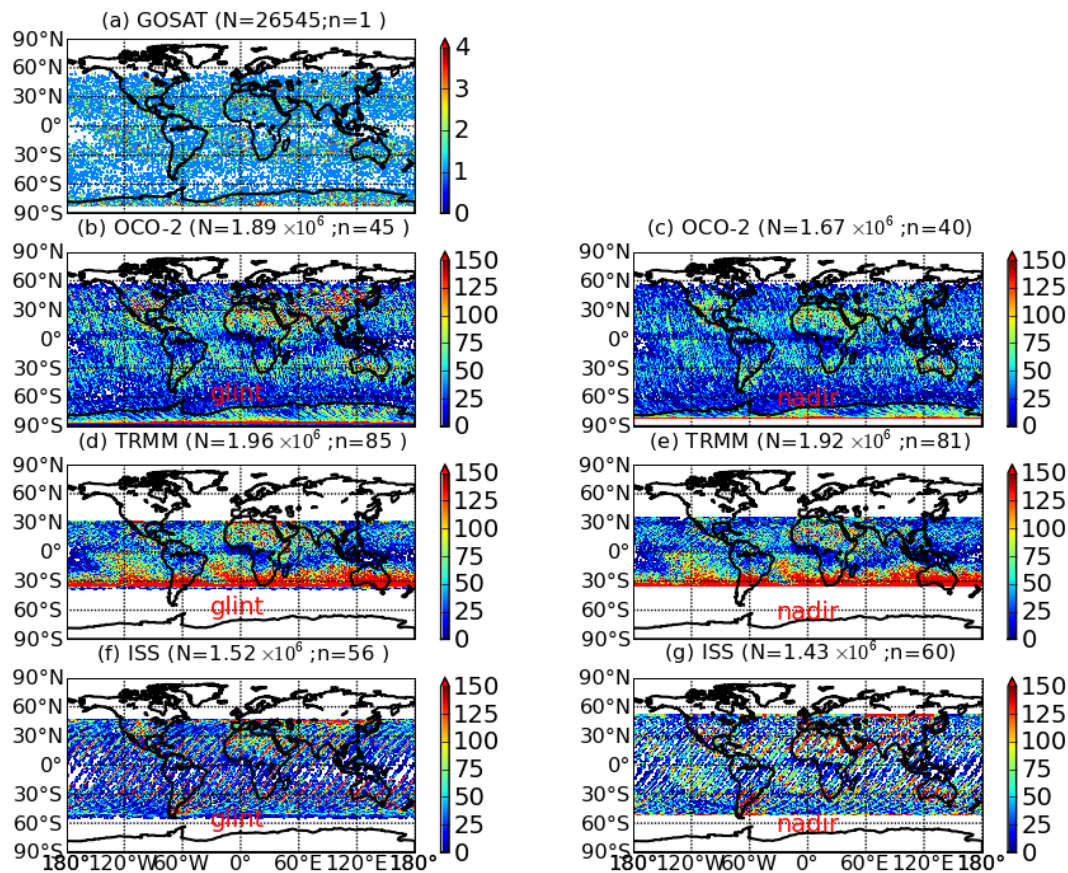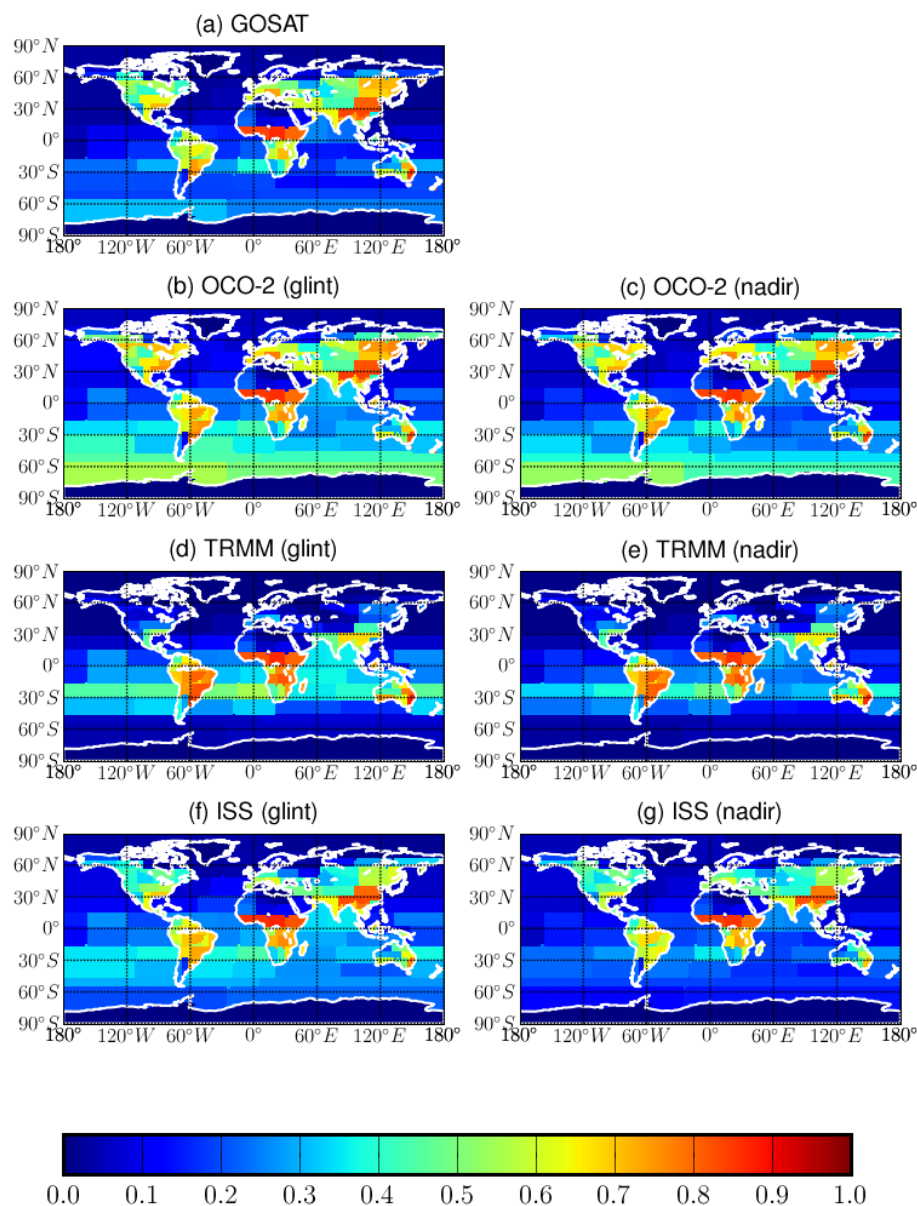
Fig. 3. The number of cloud- and aerosol- free scenes (AOD < 0.3) for January 2003 averaged on a uniform 1° grid for GOSAT and OCO-2 in sun-synchronous orbits, and for an OCO-2 SWIR spectrometer in the NASA TRMM and ISS orbits. For GOSAT we consider the sum of nadir and glint measurements, reflecting its current operational mode. N is the monthly global total clear-sky measurements, and n is mean number of clear-sky measurements for each grid box with measurements. See Table 1 for details about the orbit and instrument characteristics.

increases the probability of observing cloud-free scenes. The larger number of observations resulting from this orbit also allows a degree of redundancy in the measurement strategy, if required. The TRMM and ISS orbits precess and consequently sample different local times of day, which may provide a small amount of diurnal information (yet to be determined and outside the scope of this present work). For January 2003 between 30° S–30° N, we find that the TRMM orbit provides 1.9 million (2.0 million) nadir and glint clear-sky measurements, approximately evenly split between a.m. and p.m. daylight hours; the ISS orbit provides 1.4 million (1.5 million) nadir and glint clear-sky measurements split between a.m. and p.m. daylight hours; and for the same time and region, we find that GOSAT and OCO-2 provide 26 545 and 1.7 million (1.9 million) nadir and glint clear-sky measurements, respectively. The resulting daily mean random error for X_{CO_2} (not shown) for continents is generally well below 1 ppm, except at polar latitudes sampled by the OCO-2 orbit reflecting errors associated with snow and ice, and over the oceans at latitudes greater than

30° sampled by GOSAT reflecting its glint measurements being restricted to within ±20° of subsolar latitude.

Figure 4 shows the fractional reduction in error (γ) between the a posteriori and the a priori (Feng et al., 2009): $\gamma = 1 - \hat{\mathbf{S}}_{i,i}/\mathbf{S}^a_{i,i}$, where $\hat{\mathbf{S}}_{i,i}$ and $\mathbf{S}^a_{i,i}$ correspond to the i-th diagonal entry of the a posteriori and a priori error covariance matrices, respectively. For this calculation we distinguish, except for GOSAT as explained above, between the error reduction due to using nadir and glint measurements. For the OCO-2 orbit, the largest error reductions due to nadir and glint measurements are over the continents, as expected. The glint measurements also make a significant impact over the ocean, as previously reported (Feng et al., 2009; Baker et al., 2010). A similar distribution of error reduction is shown for the GOSAT measurements but the reduction in error is typically smaller. We find that over some regions, e.g. western China, GOSAT shows greater improvement in flux uncertainties, reflecting spatial correlations in model transport error that favour a sparser distribution of measurements, as discussed above. For the ISS orbit, we find

Fig. 4. The fractional error reduction γ of surface CO$_2$ fluxes for January 2003, averaged over 144 regions defined by the Transcom-3 regions (Feng et al., 2009), for GOSAT and OCO-2 in sun-synchronous orbits, and for an OCO-2 SWIR spectrometer in the NASA TRMM and ISS orbits. For GOSAT we consider the sum of nadir and glint measurements, reflecting its current operational mode. The error reduction is calculated as $\gamma = 1 - \hat{S}_{i,i}/S_{i,i}^{a}$, where $\hat{S}_{i,i}$ and $S_{i,i}^{a}$ correspond to the i-th diagonal entry of the a posteriori and a priori error covariance matrices, respectively. For the purpose of this calculation we distinguish between OCO-2 nadir (left panels) and glint measurements (right panels).

substantial reductions in error, mainly limited to tropical latitudes for the nadir measurements but reasonably widespread for glint measurements. The TRMM orbit shows the largest error reductions over tropical land and oceans, reflecting the larger number of measurements. The increase in γ for TRMM compared to OCO-2 is not as large as would be expected due to a saturation effect in which the number of measurements per grid box required to significantly reduce

uncertainty ($\simeq$20 for the spatial resolution of the control calculations) is already reached by OCO-2 for the spatial resolution of the fluxes shown. The TRMM data also reduces errors over the extratropics, reflecting atmospheric transport. Figure 5 shows the results from a sensitivity calculation for γ using glint measurements that assumes a shorter correlation length scale (50 km) for the measurement and model errors representative of anticipated future improvements in
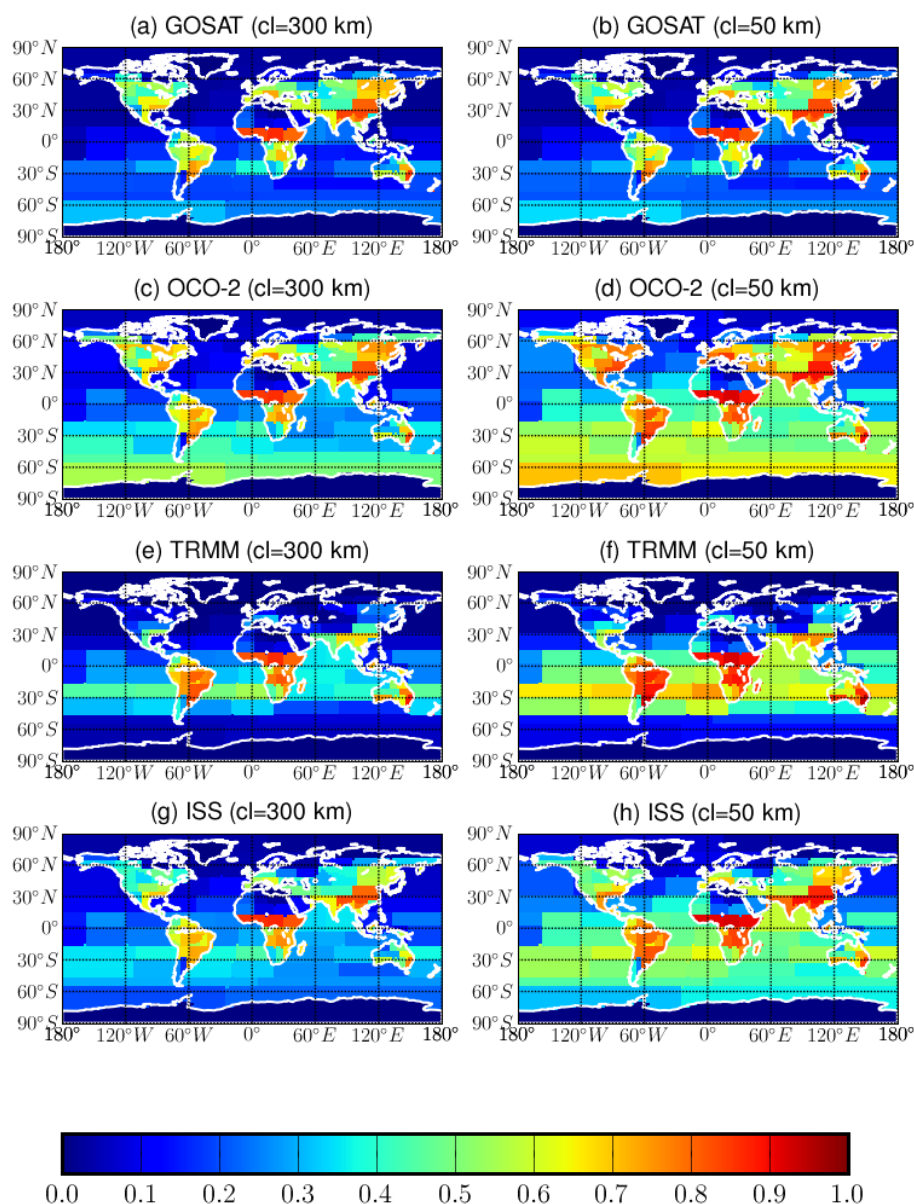
Fig. 5. Same as Fig. 4 but here we consider only glint measurements and include a spatial measurement and model error correlation length of 300 km (left panels) and 50 km (right panels).

transport models. We generally find this improves flux estimates, except for GOSAT which is insensitive to the shorter length scale because of its sparse measurement distribution. The largest improvements are for TRMM and ISS, which have highest measurement densities, as expected.

Figure 6 assesses the achievable spatial resolution of inferred fluxes, assuming an error correlation scale of 300 km, using observations from OCO-2, TRMM, ISS, and GOSAT orbits, by estimating tropical South American surface CO$_2$ fluxes resolved at different horizontal spatial resolutions. First, we estimate fluxes at a spatial resolution of $2° \times 2.5°$ and aggregate these fluxes to coarser resolutions

of $4° \times 5°$, $6° \times 7.5°$, $8° \times 10°$, $10° \times 12.5°$, $12° \times 15°$, and $14° \times 17.5°$, corresponding to length scales of 0.05, 0.2, 0.5, 1.0, 1.5, 2.0, and 3.0×10^6 km^2, respectively. We only consider values of γ above 0.5 so that the state vector is less influenced by a priori assumptions (Rodgers, 2000); we acknowledge this is not a perfect metric but it is useful to comparatively assess the different concepts. We find that cloud- and aerosol- free (AOD < 0.3) OCO-2 measurements over South America reach the $\gamma = 0.5$ level at $\simeq 9.0 \times 10^5$ km^2, corresponding to a horizontal length scale of $\simeq 950$ km. For GOSAT and ISS, $\gamma = 0.5$ is reached at 2.4×10^6 km^2 and 1.1×10^6 km^2, corresponding to horizontal length scales of
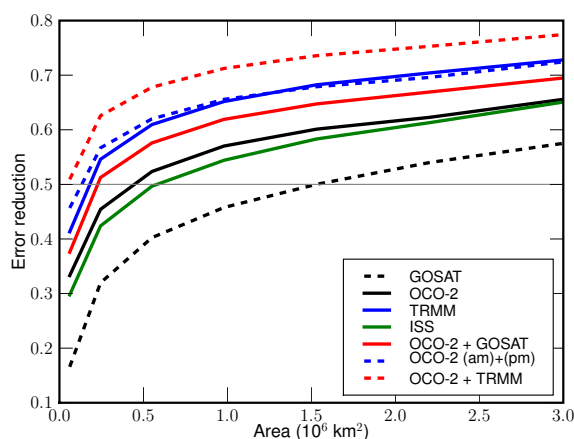
Fig. 6. The fractional error reduction γ of surface CO$_2$ fluxes over South America (15° S–15° N) during January 2003 as a function of spatial resolution: 0.05, 0.2, 0.5, 1.0, 1.5, 2.0, and 3.0×10^6 km^2, respectively. We consider the error reduction using glint measurements from OCO-2 and GOSAT in sun-synchronous orbits, and for an OCO-2 SWIR spectrometer in the NASA TRMM and ISS orbits. The horizontal line denotes the $\gamma = 0.5$ value.

1530 km and 1020 km, respectively. For the TRMM orbit, we can estimate fluxes down to 4×10^5 km^2 corresponding to a horizontal length scale of $\simeq 630$ km. We find that reducing the measurement and model error correlation length scale from 300 km to 50 km, as described above, increases the performance of OCO-2 ($\gamma = 0.5$ from 950 km to 663 km) and of TRMM ($\gamma = 0.5$ from 630 km to 412 km).

We also consider the impact of combining OCO-2 (ascending orbit) with (1) an OCO-2 in a descending orbit, (2) GOSAT (descending) and (3) with TRMM. For these calculations, we assumed no error correlation between measurements taken by two instruments, but acknowledge some correlation will result from including model transport error. Figure 6 shows that combining OCO-2 and GOSAT is comparable with results from using only the TRMM orbit, with the improvement in performance due to additional spatial coverage for each 8-day period. Combining ascending and descending OCO-2 instruments leads to marginally better results than the TRMM concept. Combining OCO-2 and TRMM outperforms any individual mission concept with independent flux estimates available on a horizontal length scale of 400 km. If we consider a shorter model error correlation of 50 km, we find this combined experiment could estimate fluxes on length scales < 300 km, approaching those achievable by concentration data collected by regional aircraft.

To assess the temporal resolution of spatially resolved CO$_2$ fluxes supported by OCO-2 and TRMM, we inferred fluxes over 4 and 8 day intervals for 0.05, 0.2, 0.5, 1.0, 1.5, 2.0, and 3.0×10^6 km^2. We find that for OCO-2 the $\gamma = 0.5$ metric increases the spatial dimension by 31 % as the temporal resolution increases from 8 day to 4 days. For TRMM, we

find that the $\gamma = 0.5$ metric increases the spatial dimension by only 4 % for the same increase in temporal resolution, again reflecting the high measurement density and the saturation effect previously mentioned.

5 Conclusions

This paper describes the foundations of a space-based carbon mission for better understanding the magnitude, spatial and temporal distribution and durability of tropical carbon fluxes. We have focused our attention on the tropics because it is one of two broad geographical regions that are characterized with large uncertainty, the other being the boreal region. We recognise that a clear case of support could be developed that focused on either region. For either region, the focus would be to characterize the natural biosphere fluxes which are expected to imprint only a diffuse signature on a X_{CO_2} measurement so that maximizing the measurement density is critical. However, we also show that spatial correlated measurement and model errors can reduce the effectiveness of measurement density. We show that the precessing orbit provides 120 % more clear-sky measurements over the tropics than the sun-synchronous orbit, resulting in a 34 % increase in horizontal resolution of carbon fluxes that can be independently inferred.

We have used a low-inclination, precessing orbit, based on orbital parameters previously used by the NASA TRMM mission that focused on tropical rainfall weather systems, which restricts the orbit between $\simeq \pm 35°$ in latitude. These parameters can be optimized to focus on, for example, a narrower range of latitudes or maximize the repeat frequency of measurements, subject to engineering constraints. One of the major advantages and disadvantages of using a precessing orbit is the varying local time of measurements. The advantage is that we could these data to build up a coarse diurnal cycle of surface fluxes, in theory subject to dilution due to atmospheric mixing processes, but the disadvantage of these data is that they are difficult to interpret without a transport model and data assimilation system. Previous analysis of the precipitation radar data from the TRMM orbit showed that even hourly data over three years was inadequate to describe the diurnal cycle on spatial scales less than 12° (approximately 1.4×10^6 km^2) due to variability in sampling (Negri et al., 2002). However, in the case of trace gases with lifetimes of more than a few weeks we anticipate that sampling variability makes little difference. For such gases, column measurements are already a superposition of the target gas emitted from different processes, geographical regions, and from different local times (Palmer et al., 2008). The extent to which we can determine a diurnal cycle, e.g. over a particular spatial or temporal extent, is outside the scope of this present study and the subject of ongoing work.

In this paper, we have focused on daytime SWIR measurements of CO$_2$. The precessing orbit does pass through

nighttime local hours and consequently to take full advantage of the orbit we would also consider TIR wavelengths. During the daytime SWIR and TIR measurements could be used to provide some vertical resolution for CO_2 (Christi and Stephens, 2004) and during the night these data can be used to test atmospheric transport (e.g. Chahine et al., 2008). Here, we have only considered CO_2 trace gas measurements but previous studies have emphasized the importance of coincident measurements of CO to improve flux attribution (e.g. Palmer et al., 2006). Prevalent cirrus clouds in the tropics (Dessler and Yang, 2003) can be characterised by an imager aboard the satellite.

Finally, we have also showed the benefit of using two similar instruments, one in a sun-synchronous (global survey) orbit and one focused on the tropics. By better constraining tropical CO_2 fluxes we indirectly increase the efficacy of high latitude measurement constraints. With the unarguable science and economic benefits of better understanding CO_2 fluxes, we may have to optimize instrument and orbit parameters to address both applications. Using satellite instruments to help verify emission treaties may require different orbital characteristics, e.g. denser measurements in space and/or time.

Appendix A

Cloud screening

We determine cloud-free observations by sampling 3-hourly ECMWF operational analysis for total cloud coverage at $0.25° \times 0.25°$ regular latitude-longitude grid boxes.

For simplicity, we approximate the dependence of the probability for a cloud-free observation on its pixel size s and the cloud coverage P_c of the co-located $0.25° \times 0.25°$ grid box by using:

$$f(P_c, s) = F_p(s)\, g_o(1 - P_c), \tag{A1}$$

where g_o defined as a constant factor for alignment between the instrument pixel and the cloud-free sub-grid region, which we choose to be 0.8 for OCO-2 and 1.0 for GOSAT due its pixel size (about $100\,km^2$). As a result, about 16 % of OCO-2 nadir observations (of effective pixel size about $3\,km^2$) between 60° S and 60° N are determined to be cloud-free, and about 10 % GOSAT nadir observations are cloud-free. We acknowledge that using a constant alignment factor g_o will lead to overestimation of the probability for cloud-free observations at high (i.e. large P_c) cloud coverage, and underestimation at low cloud coverage. $F_p(s)$ is the penalty function accounting for the adverse effects on cloud-free probability when the effective instrument pixel size is larger than the nominal $1\,km^2$ (Bösch et al., 2011):

$$F_p(s) = \frac{26.098\, s^{-0.45} + 10.18}{26.098 + 10.18}. \tag{A2}$$

We produce a pseudo-random number between 0 and 1, and compare it with the calculated cloud-free probability from Eq. (A1) to determine whether a single observation is cloud-free. If necessary (for OCO-2 instruments), we repeat the generation of pseudo-random numbers for multiple co-located observations to calculate the number of cloud-free observations at each $0.25° \times 0.25°$ grid box. To correct the overestimation at large cloud coverage, further penalty is applied to ensure that the area covered by clear observations is smaller than cloud-free sub-grid regions given by ECMWF analysis.

Appendix B

Including spatially correlated errors in an ensemble Kalman filter

In our EnKF approach, uncertainties associated with a priori state vector x^f (i.e the surface fluxes) are represented by an ensemble of perturbations states Δx^f so that the a priori error covariance matrix $\mathbf{P}^f$ is approximated by: $\mathbf{P}^f = \Delta x^f (\Delta x^f)^T$.

By optimally fitting model values to the (simulated) X_{CO_2} observations y_{obs}, we obtain the a posteriori state vector x^a by using:

$$x^a = x^f + \mathbf{K}_e \left[y_{obs} - H(x^f) \right], \tag{B1}$$

where x^f and x^a are the a priori and a posteriori state vectors; $H(x^f)$ is the model observations, and H is the observation operator that describes the relationship between the state vector and the observations. H accounts for surface fluxes and the global atmospheric CO_2 transport during each assimilation lag window, interpolating the resulting 3-D CO_2 fields to the observation locations, and convolving CO_2 profiles to X_{CO_2} using averaging kernels.

In our previous study (Feng et al., 2009), we calculate the ensemble gain matrix $\mathbf{K}_e$ using:

$$\mathbf{K}_e = \Delta x^f (\Delta Y)^T \left[\Delta Y (\Delta Y)^T + \mathbf{R} \right]^{-1}, \tag{B2}$$

where $\mathbf{R}$ is the observation error covariance, and ΔY is defined as $\Delta Y = H(\Delta x^f)$. When observation number is small and $\mathbf{R}$ has a simple structure (i.e. diagonal) so that $\mathbf{R}^{-1/2}$ can be easily found, $\mathbf{K}_e$ can be efficiently calculated via singular value decomposition (SVD) of matrix $(Y)^T \mathbf{R}^{-1/2}$.

In the current study, because we have included observation error correlations across several thousand clear-sky observations for each day, calculation of $\mathbf{R}^{-1/2}$ is no longer trivial. To avoid the direct calculation of $\mathbf{K}_e$ we determine a matrix $\mathbf{Y}_c$ by solving the linear equation

$$\left[\Delta Y (\Delta Y)^T + \mathbf{R} \right] \mathbf{Y}_c = y_{obs} - H\left(x^f \right), \tag{B3}$$

which can be solved efficiently by using LU decomposition ideal for the sparse matrix $\Delta Y (\Delta Y)^T + \mathbf{R}$. As a result, the a posteriori is now given by

$$\boldsymbol{x}^{\mathrm{a}} = \boldsymbol{x}^{\mathrm{f}} + \Delta \boldsymbol{x}^{\mathrm{f}} (\Delta Y)^T \, \mathbf{Y}_{\mathrm{c}}. \tag{B4}$$

The number of observations and the off-diagonal structure of $\mathbf{R}$ also makes it difficult to use the SVD technique to calculate transform matrix $\mathbf{T}$. However, the matrix $\mathbf{I} + \Delta Y^T \mathbf{R}^{-1} \Delta Y$ has the dimension of the state vector, which is much smaller than the number of observations. Its inversion (and square root) can be calculated efficiently once we have determined the term $\Delta Y^T \mathbf{R}^{-1} \Delta Y$ numerically. We avoid the inversion of matrix $\mathbf{R}^{-1}$ by choosing to first determine matrix $\mathbf{Z} = \mathbf{R}^{-1} \Delta Y$ and using LU decomposition to solve the linear equation $\mathbf{R} \mathbf{Z} = \Delta Y$.

References

Baker, D. F., Bösch, H., Doney, S. C., O'Brien, D., and Schimel, D. S.: Carbon source/sink information provided by column CO$_2$ measurements from the Orbiting Carbon Observatory, Atmos. Chem. Phys., 10, 4145–4165, doi:10.5194/acp-10-4145-2010, 2010.

Bösch, H., Baker, D., Connor, B., Crisp, D., and Miller, C.: Global Characterization of X$_{\mathrm{CO_2}}$ Retrievals from Shortwave-infrared satellite observation of the Orbiting Carbon Observatory-2 Mission, Remote Sens., 11, 270–304, doi:10.3390/rs3020270, 2011.

Chahine, M. T., Chen, L., Dimotakis, P., Jiang, X., Li, Q., Olsen, E. T., Pagano, T., Randerson, J., and Yung, Y. L.: Satellite remote sounding of mid-tropospheric CO$_2$, Geophys. Res. Lett., 35, L17807, doi:10.1029/2008GL035022, 2008.

Chevallier, F., Feng, L., Bösch, H., Palmer, P. I., Rayner, P. J.: On the impact of transport model errors for the estimation of CO$_2$ surface fluxes from GOSAT observations, Geophys. Res. Lett., 37, L21803, doi:10.1029/2010GL044652, 2010.

Christi, M. J. and Stephens, G. L.: Retrieving profiles of atmospheric CO$_2$ in clear sky and in the presence of thin cloud using spectroscopy from the near and thermal infrared: a preliminary case study, J. Geophys. Res., 109, D04316, doi:10.1029/2003JD004058, 2004.

Crisp, D., Atlas, R. M., Breon, F.-M., Brown, L. R., Burrows, J. P., Ciais, P., Connor, B. J., Doney, S. C., Fung, I. Y., Jacob, D. J., Miller, C. E., O'Brien, D., Pawson, S., Randerson, J. T., Rayner, P., Salawich, R. J., Sander, S. P., Sen, B., Stephens, G. L., Tans, P. P., Toon, G. C., Wennberg, P. O., Wofsy, S. C., Yung, Y. L., Kuang, Z., Chudsama, B., Sprague, G., Weiss, B., Pollock,

R., Kenyon, D., Schroll, S.: The Orbiting Carbon Observatory (OCO) Mission, Adv. Space. Res., 34, 700–709, 2004.

Dessler, A. E. and Yang, P.: The distribution of tropical thin cirrus clouds inferred from Terra MODIS data, J. Climate, 16, 1241–1247, 2003.

Feng, L., Palmer, P. I., Bösch, H., and Dance, S.: Estimating surface CO$_2$ fluxes from space-borne CO$_2$ dry air mole fraction observations using an ensemble Kalman Filter, Atmos. Chem. Phys., 9, 2619–2633, doi:10.5194/acp-9-2619-2009, 2009.

Feng, L., Palmer, P. I., Yang, Y., Yantosca, R. M., Kawa, S. R., Paris, J.-D., Matsueda, H., and Machida, T.: Evaluating a 3-D transport model of atmospheric CO$_2$ using ground-based, aircraft, and space-borne data, Atmos. Chem. Phys., 11, 2789–2803, doi:10.5194/acp-11-2789-2011, 2011.

Gurney, R. G., Law, R. M., Denning, A. S., Rayner, P. J., Baker, D., Bousquet, P., Bruhwiler, L., Chen, Y.-H., Ciais, P., Fan, S., Fung, I. Y., Gloor, M., Heimann, M., Higuchi, K., John, J., Maki, T., Maksyutov, S., Masarie, K., Peylin, P., Prather, M., Pak, B. C., Randerson, J., Sarmiento, J., Taguchi, S., Takahashi, T., and Yuen, C.-W.: Towards robust regional estimates of CO$_2$ sources and sinks using atmospheric transport models, Nature, 415, 626–630, 2002.

Hungershoefer, K., Breon, F.-M., Peylin, P., Chevallier, F., Rayner, P., Klonecki, A., Houweling, S., and Marshall, J.: Evaluation of various observing systems for the global monitoring of CO$_2$ surface fluxes, Atmos. Chem. Phys., 10, 10503–10520, doi:10.5194/acp-10-10503-2010, 2010.

Kuze, A., Suto, H., Nakajima, M., and Hamazaki, T.: Thermal and near infrared sensor for carbon observation fourier-transform spectrometer on the greenhouse gases observing satellite for greenhouse gases monitoring, Appl. Optics, 48, 6717–6733, 2009.

Law, R. M., Chen, Y. H., and Gurney, K. R.: TransCom 3 CO$_2$ inversion intercomparison: 2. Sensitivity of annual mean results to data choices, Tellus B, 55, 580–595, 2003.

Le Quere, C., Raupach, M. R., Marland, J. G. C. G., Bopp, L., Ciais, P., Conway, T. J., Doney, S. C., Feely, R. A., Foster, P., Friedlingstein, P., Gurney, K., Houghton, R. A., House, J. I., Huntingford, C., Levy, P. E., Lomas, M. R., Majkut, J., Metzl, N., Ometto, J. P., Peters, G. P., Prentice, I. C., Randerson, J. T., Running, S. W., Sarmiento, J. L., Schuster, U., Sitch, S., Takahashi, T., Viovy, N., van Der Werf, G. R., and Woodward, F. I.: Trends in the sources and sinks of carbon dioxide, Nat. Geosci., 2, 831–836, 2009.

Lin, J. C., Gerbig, C., Daube, B. C., Wofsy, S. C., Andrews, A. E., Vay, S. A., and Anderson, B. E.: An empirical analysis of the spatial variability of atmospheric CO$_2$: implications for inverse analyses and space-borne sensors, Geophys. Res. Lett., 31, L23104, doi:10.1029/2004GL020957, 2004.

Marland, G., Boden, T. A., and Andres, R. J.: Global, Regional, And National CO$_2$ Emissions, in Trends: A Compendium of Data on Global Change, Tech. Rep. 2007. 7346, Carbon Dioxide Information Analysis Center Oak Ridge National Laboratory, US Department of Energy, Oak Ridge, Tenn., USA, 2007.

Miller, C. E., Crisp, D., DeCola, P. L., Olsen, S. C., Randerson, J. T., Michalak, A. M., Alkhaled, A., Rayner, P., Jacob, D. J., Suntharalingam, P., Jones, D. B. A., Denning, A. S., Nicholls, M. E., Doney, S. C., Pawson, S., Boesch, H., Connor, B. J., Fung, I. Y., O'Brien, D., Salawitch, R. J., Sander, S. P., Sen, B., Tans, P., Toon, G. C., Wennberg, P. O., Wofsy, S. C., Yung, Y. L., and

Law, R. M.: Precision requirements for space-based X_{CO_2} data, J. Geophys. Res, D10314, doi:10.1029/2006JD007659, 2007.

Negri, A. J., Bell, T. L., and Xu, L.: Sampling of the diurnal cycle of precipitation using TRMM, J. Atmos. Ocean. Tech., 19, 1333–1344, 2002.

Palmer, P. I., Suntharalingam, P., Jones, D. B. A., Jacob, D. J., Streets, D. G., Fu, Q., Vay, S. A., and Sachse, G. W.: Using CO_2:CO correlations to improve inverse analyses of carbon fluxes, J. Geophys. Res., 111, D12318, doi:10.1029/2005JD006697, 2006.

Palmer, P. I., Barkley, M. P., and Monks, P. S.: Interpreting the variability of space-borne CO_2 column-averaged volume mixing ratios over North America using a chemistry transport model, Atmos. Chem. Phys., 8, 5855–5868, doi:10.5194/acp-8-5855-2008, 2008.

Patra, P. K., Maksyutov, S., Sasano, Y., Nakajima, H., Inoue, G., and Nakazawa, T.: An evaluation of CO_2 observations with Solar Occultation FTS for Inclined-Orbit Satellite sensor for surface source inversion, J. Geophys. Res., 108, 4759, doi:10.1029/2003JD003661, 2003.

Randerson, J. T., Thompson, M. V., Conway, T. J., Fung, I. Y., and Field, C. B.: The contribution of terrestrial sources and sinks to trends in the seasonal cycle of atmospheric carbon dioxide, Global Biogeochem. Cy., 11, 535–560, 1997.

Rodgers, C. D.: Inverse Methods for Atmospheres: Theory and Practise, World Scientific Press, 2000.

Takahashi, T., Sutherland, S., Sweeney, C., Poisson, A., Metzl, N., Tilbrook, B., Bates, N., Wanninkhof, R., Feely, R., and Sabine, C.: Global sea-air CO_2 flux based on climatological surface ocean pCO_2, and seasonal biological and temperature effects, Deep-Sea Res. Pt. II, 49, 1601–1622, 2009.

van der Werf, G. R., Randerson, J. T., Giglio, L., Collatz, G. J., Kasibhatla, P. S., and Arellano Jr., A. F.: Interannual variability in global biomass burning emissions from 1997 to 2004, Atmos. Chem. Phys., 6, 3423–3441, doi:10.5194/acp-6-3423-2006, 2006.

Yevich, R. and Logan, J. A.: An assessment of biofuel use and burning of agricultural waste in the developing world, Global Biogeochem. Cy., 17, 1095, doi:10.1029/2002GB001952, 2003.